Influence of subsurface injection on time-lapse seismic.

Laboratory studies at seismic and ultrasonic frequencies.

Dawid Szewczyk[1], Rune Martin Holt[1] & Andreas Bauer[1,2]

[1.] *Norwegian University of Science and Technology (NTNU), Department of Geoscience and Petroleum, 7491, Trondheim, Norway.*

[2.] *SINTEF Petroleum Research, Formation Physics, 7031 , Trondheim, Norway.*

Contact email: dawid.szewczyk@ntnu.no

Abstract

Seismic monitoring of reservoir and overburden performance during subsurface CO_2 storage plays a key role in ensuring efficiency and safety. Proper interpretation of monitoring data requires knowledge about the rock physical phenomena occurring in the subsurface formations. This work focuses on rock-stiffness and elastic-velocity changes of a shale overburden formation caused by both reservoir-inflation induced stress changes, and leakage of CO_2 into the overburden. In laboratory experiments, Pierre shale I core plugs were loaded along the stress path representative for the in-situ stress changes experienced by caprock during reservoir inflation. Tests were carried out in a triaxial compaction cell combining three measurement techniques and permitting for determination of: (i) ultrasonic velocities; (ii) quasi-static rock deformations, (iii) dynamic elastic stiffnesses at seismic frequencies within single test; which allowed to quantify effects of seismic dispersion. In addition fluid-substitution effects connected with possible CO_2 leakage into the caprock formation were modelled by the modified anisotropic Gassmann model. Results of this work indicate that: (i) stress sensitivity of Pierre shale I is frequency dependent; (ii) reservoir inflation leads to the increase of the overburden Young's modulus and Poisson's ratio; (iii) in-situ stress changes mostly affects the P-wave velocities; (iv) small leakage of the CO_2 into the overburden may lead to the velocity changes which are comparable with one associated with geomechanical influence; (v) non-elastic effects increase stress sensitivity of an acoustic waves; (iv) both geomechanical and fluid substitution effects would create significant time shifts which should be detectable by time-lapse seismic.

1   Introduction

In order to ensure safety, efficiency and optimization of field operations proper monitoring technique as well as correct interpretation of monitoring data is needed. During injection of fluid into a reservoir (e.g. CO_2 for storage or enhanced oil recovery) time-lapse seismic (4D) is a proven technology used for monitoring purposes. Most of the monitoring surveys and associated laboratory investigations concentrate on time shifts connected with saturation, pore pressure and stress changes in the reservoir (e.g. Landrø et al. 2003; Meadows 2008; Lumley 2010). However, it has been recognized that true shifts caused by stress and strain changes in the overburden, can also give valuable information about deformations of both reservoir and caprock (e.g. Kenter et al. 2004; Hatchell and Bourne 2005; Barkved and Kristiansen 2005). Field case studies performed by Duffaut and Landrø (2007) have shown that the 4D time shifts observed in a real case are hard to describe by a single dominant factor, and that proper interpretation of surveys requires consideration of many possible aspects. It is therefore important to understand how temperature, in-situ stress conditions and fluid distribution/substitution influence the elastic-velocities of both reservoir and overburden formations. Holt and Stenebråten (2013) performed a series of ultrasonic tests in which artificially manufactured rock samples, representative for some types of a storage rocks and a caprocks, were exposed to stress changes characteristic for reservoir and overburden in-situ conditions during reservoir depletion and inflation. Their work indicated significant velocity changes in both formations as well as possible yield of the overburden caused by associated stress changes. Holt and Stenebråten (2013) also showed that the effects of fluid substitution (in a reservoir) and stress/strain changes on the velocities may have comparable magnitudes and would be hard to distinguish during seismic data interpretation. However, as pointed out by the authors, the use of synthetic analogues can be challenged. Further, dispersion is observed in several fluid saturated rocks (e.g. Winkler and Nur 1979; Johnston and Christensen 1995; Wang 2002; Batzle et al. 2005; Duranti, Ewy and Hofmann 2005; Batzle, Han and Hofmann 2006; Mikhaltsevitch, Lebedev and Gurevich 2014; Pimienta, Fortin and Gueguen 2015), which may cause different stress sensitivity at seismic frequencies compared to

ultrasonic frequencies (Mavko and Vanorio 2010). Therefore, further examination of the problem is required.

In this work, we report on laboratory experiments in which Pierre shale I, mimicking caprock, was exposed to a generic stress path that might be representative for overburden in-situ conditions during injection into a reservoir beneath it. The experiments were performed in a set-up allowing for combined measurements of quasi-static rock deformations, ultrasonic velocities, and dynamic elastic stiffnesses at seismic frequencies, with applied pore pressure and deviatoric stresses. The primary objective of the paper is to contribute to the understanding of elastic-velocity changes in the overburden formation under reservoir inflation. However, parallel performed multi-frequency tests combined with static experiments allows to identify the influence of the seismic dispersion on stress sensitivity, as well as permits to recognize possible factors behind differences between static and dynamic properties of rocks. After a short description of the used material and the applied laboratory techniques, we present experimental results focusing on the stress sensitivity of (i) dynamic and static rock engineering parameters (Young's modulus and Poisson's ratio); and (ii) seismic and ultrasonic P- and S-wave velocities. We also model possible fluid substitution effects (within the overburden) with the use of the modified anisotropic Gassmann model, accounting for adsorption and capillary-pressure effects observed in shales (Szewczyk et al. 2017b).

2   Materials and methods

2.1. Pierre shale

Laboratory tests were conducted on a Pierre shale I core plug with a diameter of 1 inch and a length of 2 inches. Pierre shale I used in this work is an outcrop shale from North Dakota, it exhibit transverse isotropy (e.g. Islam and Skalle 2013) and is considered as an analogue for some overburden formations. Tested core plugs were drilled from outcrop material preserved in oil at $0°$ angle of inclination with respect to the symmetry axis. XRD data shows that the studied batch contains about 48 wt% clay minerals, 44 wt% silicate minerals (27 wt% quartz) and around 6 wt% of

carbonates. Due to the short sample consolidation time (strain measurements shows that, while exposing the core plugs to brine under stress, the strains stabilize within ~53 hours), as-received material is considered as nearly fully saturated. The porosity of the tested sample was not determined directly, however, based on the measured bulk density of as-received material and mineral density of its composites (taken from XRD test), we have estimated a porosity of~ 16% ± 1%. This result is in good agreement with data reported in the literature (~ 10% - 25% porosity) (e.g. Schultz et al. 1980; Olgaard, Nuesch and Urai 1995; Holt et al. 2015)

2.2. Experimental set-up

The experiments were carried out in a low frequency apparatus at the Formation Physics Laboratory of SINTEF Petroleum Research. The apparatus combines three measuring techniques that allow for determination of ultrasonic velocities, quasi-static rock deformations and dynamic elastic stiffnesses at seismic frequencies under deviatoric stresses, within single test. Design of the apparatus together with an in-house developed strain gauge fitting/sample mounting procedure allows for sealing of the core plugs within~ 1h after removing them from preservation oil, thus most likely providing maintenance of their initial state. A schematic illustration of the experimental set-up is shown in Figure 1.

[Figure 1 about here]

The sample stack consists of a loading piston, two endcaps with the sample placed in between them, a holder with a set of three linear variable displacement transducers (LVDT's) measuring displacements in the vertical direction, an aluminium piece with attached semiconductor strain gauges, a piezoelectric force sensor, a piezoelectric actuator and an internal load cell. The entire stack is placed on the bottom flange of a compaction cell equipped with electronic feed-throughs and fluid channels allowing for independent control of pore pressure and confining pressure. The compaction cell (designed for a maximum confining pressure of 70MPa) is placed inside the mechanical loading frame that exerts an axial force onto the sample. Measurements at

ultrasonic frequencies are performed by the pulse-transmission technique. Two pairs of in-house built compressional (P) and shear (S) wave transducers are embedded in the top and bottom endcaps allowing for ultrasonic velocity measurements along the sample axis. The excitation frequency used during the experiments presented in this manuscript for both P- and S-wave transducers was 500 kHz (centre frequency of the piezoelectric crystals). The received P-wave velocity signal had an average frequency of about 450 kHz, while received S-wave velocity signal had an average frequency of about 320 kHz (Figure 2a-h). The picking of the arrivals includes: (i) comparing the actual waveforms with the waveforms recorded with aluminium standard, (ii) tracking frequency related arrival time shifts obtained from waveforms acquired at several frequencies lower than 500 kHz (data recorded immediately after 500 kHz measurements), and (iii) comparing the ultrasonic data with seismic measurements. Quasi-static rock deformations were determined with the use of an internal load cell (measuring deviatoric stress), a set of three LVDT's distributed equally around the circumference of sample, and a set of four sealed foil strain-gages attached to the sample (measuring axial strain locally). Redundancy in the determination of axial deformation is used for verification purposes or identification of large heterogeneities in the sample. Finally, rock engineering properties (Young's modulus and Poisson's ratio) at seismic frequencies (1Hz-155Hz) are measured with the use of the forced-deformation method described by Spencer (1981). An amplified sinusoidal electric signal is applied to the piezoelectric displacement actuator, which results in oscillatory axial force modulations measured by the piezoelectric force sensor. In order not to exceed the elastic regime of the tested specimen the sample strains are kept below 10^{-6} (e.g. Gordon and Davis 1968; Iwasaki, Tatsuoka and Takagi 1978). Strains are measured locally with the use of 8 sealed strain gauges attached to the sample (4 measuring strains in axial direction and 4 measuring strain in radial direction). From the force, F, and strain, ε, modulation amplitudes, both Young's modulus, E, and Poisson's ratios, ν, are calculated according to the following equations:

$$E = \frac{\Delta\sigma_{ax}}{\Delta\varepsilon_{ax}} = \frac{\Delta F_{ax}}{A \cdot \Delta\varepsilon_{ax}} \text{ , and } \nu = -\frac{\Delta\varepsilon_{rad}}{\Delta\varepsilon_{ax}} \qquad (1)$$

where *A* is the cross-section area of the sample, and the indices *ax* and *rad* indicate axial and radial direction, respectively. The low frequency experimental errors were quantified with the help of standard materials (aluminium and PEEK) and are smaller than 5%. More details about experimental set-up and strain gauge fitting/sample mounting procedures are given in Szewczyk, Bauer and Holt (2016).

2.3. Experimental conditions

According to the linear elastic nucleus of strain model introduced by Geertsma (1973), for an isotropic homogenous subsurface, the mean stress remains constant in the overburden during reservoir depletion or inflation (constant mean stress (CMS) loading). This implies that the overburden above centre of the reservoir will experience a decrease in horizontal stress and increase in vertical stress, as a response to injection into a reservoir. At the edge of the storage site, the response is opposite, i.e. an increase in horizontal stress and a decrease in vertical stress. In order to simulate those effects, we have performed an experiment in which a Pierre shale core plug was loaded according to the idealized stress path characteristic for caprock above the centre of a reservoir (Figure 2i). First, the sample was loaded hydrostatically to 5 MPa confining pressure. Next, confining pressure, axial stress, and pore pressure were increased simultaneously to 19,5 MPa, 21 MPa and 2 MPa respectively. Subsequently, after sample has stabilized (which took around 53 hours), a CMS loading cycle was performed to simulate the effect of reservoir inflation. Here, the axial stress was increased by 5 MPa, and the confining pressure was reduced by 2.5 MPa to keep the mean stress constant. It is known that properties measured during first loading differ from those obtained during subsequent loading cycles (e.g. Walsh 1965). For this reason, a second CMS cycle was performed. After each loading/unloading step we have allowed the sample to stabilize before conducting low-frequency and ultrasonic measurements (the stabilization time was varying between 4 to 10 hours). After the second CMS loading cycle the axial stress was gradually reduced to 19 MPa while holding the confining pressure constant at 17 MPa (triaxial unloading). This phase of the

experiment was used to determine quasi-static properties of Pierre shale. Finally, to assure that the experiments were not executed close to the material failure, the axial load was increased with simultaneous reduction of the confining pressure until the stress state of 31 MPa axial load and 14.5 MPa confining pressure was reached (not shown in Figure 2i). During this step shale did not fail. For all loading/unloading stages, the applied loading rate was equal to 5 MPa/h for all stresses and pressures, which corresponds to the axial strain rates between $3{,}7 \cdot 10^{-7} s^{-1}$ and $5{,}5 \cdot 10^{-7} s^{-1}$. All segments of the experiments were conducted under drained conditions (assured by a metal mesh wrapped around the sample and covering about 60% - 70% of the sample's lateral surface), with 3.5% NaCl brine as a pore fluid, at a constant pore-pressure of 2 MPa. It should be noted however, that at the time scale of typical 4D seismic surveys, shale formations in the field are usually considered undrained, which implies pore pressure change. However, during CMS loading, the pore pressure change is usually small, and for the Pierre shale we can roughly estimate the pore pressure change to be between 10% and 25% of the axial stress change (Skempton 1954; Holt et al. 2015).

[Figure 2 about here]

2.4. Conversion between properties measured at seismic and ultrasonic frequencies

While velocities measured at ultrasonic frequencies are functions of P- and S- wave moduli, the low-frequency technique provides a direct measurement of Young's modulus, E, and Poisson's ratio, ν, for a given loading direction. Therefore, in order to compare results obtained at seismic and ultrasonic frequencies, conversion between those different types of moduli is required. A transversely isotropic material is characterized by 5 independent parameters forming the stiffness tensor, C$_{ijkl}$, that relates the stress tensor, σ_{ij}, and the strain tensor, ε_{kl}, of any elastic material (Hooke's law):

$$\sigma_{ij} = C_{ijkl}\varepsilon_{kl} , \tag{2}$$

where Einstein's summation convention applies. The elastic stiffness tensor (assuming that the z- axis is the symmetry axis), can be written as a matrix using Voigt notation (Voigt 1928; Nye 1985):

$$C_{ij} = \begin{bmatrix} C_{11} & C_{12} & C_{13} & 0 & 0 & 0 \\ C_{12} & C_{11} & C_{13} & 0 & 0 & 0 \\ C_{13} & C_{13} & C_{33} & 0 & 0 & 0 \\ 0 & 0 & 0 & C_{44} & 0 & 0 \\ 0 & 0 & 0 & 0 & C_{44} & 0 \\ 0 & 0 & 0 & 0 & 0 & C_{66} \end{bmatrix},$$

(3)

with $C_{12} = C_{11} - 2C_{66}$.

The anisotropy of a material can be characterized by three parameters introduced by Thomsen (1986):

$$\varepsilon = \frac{C_{11} - C_{33}}{2C_{33}},$$

(4)

$$\gamma = \frac{C_{66} - C_{44}}{2C_{44}},$$

(5)

$$\delta = \frac{(C_{13} + C_{44})^2 - (C_{33} - C_{44})^2}{2C_{33}(C_{33} - C_{44})}.$$

(6)

In conventional compaction cells, where only biaxial stresses can be applied (axial stress and confining pressure), and only axial properties measured, determination of all 5 independent stiffness parameters (C_{11}, C_{33}, C_{44}, C_{66}, C_{13}) requires the repetition of experiments on three differently oriented samples: (i) specimens drilled at 0° angle of inclination with respect to the symmetry axis; (ii) samples drilled at 90° with respect to the axis of symmetry; (iii) finally samples cut under oblique angle with respect to the symmetry axis. The equations that form the basis for inversion of laboratory data for the 5 independent stiffness parameters are (e.g. Helbig 1994; Mavko, Mukerji and Dvorkin 2009):

a) For properties acquired at ultrasonic frequencies:

$$V_{PV} = \sqrt{\frac{C_{33}}{\rho}},$$

(7)

$$V_{SV} = \sqrt{\frac{C_{44}}{\rho}},$$

(8)

$$V_{PH} = \sqrt{\frac{C_{11}}{\rho}},$$

(9)

$$V_{SH} = \sqrt{\frac{C_{66}}{\rho}}, \tag{10}$$

$$V_{qP}(\theta) = \sqrt{\frac{C_{11}sin^2\theta + C_{33}cos^2\theta + C_{44} + \sqrt{[(C_{11}-C_{44})sin^2\theta - (C_{33}-C_{44})cos^2\theta]^2 + 4[C_{13}+C_{44}]^2 sin^2\theta cos^2\theta}}{2\rho}}, \tag{11}$$

$$V_{qS}(\theta) = \sqrt{\frac{C_{11}sin^2\theta + C_{33}cos^2\theta + C_{44} - \sqrt{[(C_{11}-C_{44})sin^2\theta - (C_{33}-C_{44})cos^2\theta]^2 + 4[C_{13}+C_{44}]^2 sin^2\theta cos^2\theta}}{2\rho}}, \tag{12}$$

where ρ denotes bulk density, P and S stands for compressional and shear waves respectively, and $V_{qP}(\theta)$ and $V_{qS}(\theta)$ represent phase velocities of "quasi P-waves" and "quasi S-waves" with wave-fronts normal oriented at angle θ with respect to the symmetry axis. Subscript V denotes the direction of the symmetry axis, while subscript H denotes direction within the symmetry plane.

b) For properties acquired at seismic frequencies:

$$E_V = C_{33} - \frac{C_{13}^2}{C_{11}-C_{66}}, \tag{13}$$

$$\nu_{VH} = \frac{C_{13}}{2(C_{11}-C_{66})}, \tag{14}$$

$$E_H = \frac{4C_{66}[(C_{11}-C_{66})C_{33}-C_{13}^2]}{C_{11}C_{33}-C_{13}^2}, \tag{15}$$

$$\nu_{HV} = \frac{2C_{66}C_{13}}{C_{11}C_{33}-C_{13}^2}, \tag{16}$$

$$\nu_{HH} = \frac{(C_{11}-2C_{66})C_{33}-C_{13}^2}{C_{11}C_{33}-C_{13}^2}, \tag{17}$$

$$\frac{1}{E(\theta)} = \frac{cos^4\theta}{E_V} + \frac{sin^4\theta}{E_H} + \frac{sin^2\theta cos^2\theta[(C_{11}-C_{66})C_{33}-(C_{13}+C_{44})C_{13}]}{C_{44}[(C_{11}-C_{66})C_{33}-C_{13}^2]}, \tag{18}$$

In the present work, since the tested core plug was oriented at 0° with respect to the symmetry axis, only vertical (quasi-static, low frequency and ultrasonic) responses to the applied stress path were measured. However, if the Thomsen parameters and vertical properties of tested specimens are known, equations (4) - (6) together with equations (7) – (8) for ultrasonic measurements, and equations (13) – (14) for seismic-frequency measurements, can be inverted for

the 5 independent stiffness parameters characteristic for a given frequency. This procedure leads to two independent solutions. The choice of the physically valid solution may be achieved from TI material energy considerations, which implies the following inequalities (Nye 1985):

$$C_{44} > 0; \ C_{66} > 0; \ C_{33} > 0; \ C_{11} > C_{66} > 0; \ (C_{11} - C_{66})C_{33} - C_{13}^2 > 0. \tag{19}$$

In the following, values of Thomsen parameters representative for our specimen at seismic frequencies were assumed to be identical with the one obtained from Pierre shale field measurements at 950 ft depth performed by White, Martineau-Nicoletis and Monash (1983): $\varepsilon \approx$ 0.01, $\gamma \approx 0.03$, $\delta \approx 0.04$. At ultrasonic frequencies, Thomsen's parameters were previously measured on samples cut from the same batch of material by Holt et al. (2015): $\varepsilon \approx 0.13$, $\gamma \approx 0.25$, $\delta \approx 0.1$. Possible errors associated with this approach will be discussed later.

3   Experimental results

3.1. Rock mechanical properties

Measured static and dynamic rock mechanical properties of Pierre shale I (vertical Young's modulus, E_V, and vertical Poisson's ratio, v_{VH}) obtained during both CMS cycles as well as during triaxial unloading are shown in Figure 3 and summarized in Table 1. Data points in the seismic range were measured directly while ultrasonic parameters were calculated from measured P- and S-wave velocities. Solid lines in the figure represent a manual Cole-Cole fits (phenomenological model originally developed for the frequency dependence of the complex dielectric constant that has also been used to describe mechanical relaxation in a visco-elastic materials) (Cole and Cole 1941):

$$E' = E_\infty + \frac{E_0 - E_\infty}{2}\left[1 - \frac{sinh(1-\alpha)\ln\omega\tau_0}{cosh(1-\alpha)\ln\omega\tau_0 + cos\frac{\alpha\pi}{2}}\right], \tag{20}$$

$$E'' = \frac{\frac{E_0 - E_\infty}{2}cos\frac{\alpha\pi}{2}}{cosh(1-\alpha)\ln\omega\tau_0 + sin\frac{\alpha\pi}{2}}, \tag{21}$$

where E_∞, E_0 are high- and low- frequency moduli, τ_0 is the relaxation time, E' and E'' stand for real and imaginary part of complex modulus, ω is angular frequency and α is a parameter controlling the width of the relaxation time distribution. Open symbols at ultrasonic frequencies represent isotropic conversion from velocities to rock engineering parameters and were added to illustrate the effect of anisotropy, and the error associated with neglecting material anisotropy.

[Figure 3 about here]

Figure 3 (a,b) shows data obtained during initial CMS loading (indicated with numbers 1 and 2 in Figure 2i). Rather large seismic dispersion (about 36%) is observed for vertical Young's modulus at the reference stress state. In case of shales large dispersion is not unusual and in some cases may exceed 50% in Young's modulus (Suarez-Rivera *et al*., 2001; Duranti *et al*., 2005, Szewczyk et al. 2016) which indicates the importance of accounting for dispersion effects during seismic data interpretation. Simulated reservoir inflation leads to the stiffening of the sample in both frequency regimes. Note however, that the responses are different at seismic and ultrasonic frequencies. While at 1 Hz Young's modulus increases by around 0.2 GPa, the change at ultrasonic frequency is about 2 times smaller (see Table 1). Frequency dependent stress sensitivity of Young's modulus results, during loading, in a decrease of seismic dispersion. Different stress sensitivities at seismic and ultrasonic frequencies were observed before in relatively dry Pierre shale (Holt et al. 2016) and Mancos shale subjected to isotropic loading (Szewczyk, Bauer and Holt 2017a).

The quasi-static vertical Young's modulus (equal to E_{static} = 5.5 GPa) shown in Figure 3 (a) was obtained from the average slope of the stress-strain curve during triaxial unloading (indicated with number 5 in Figure 2i). A clear difference of around 27% between quasi-static and low frequency (1 Hz) dynamic rock stiffness is observed. The static stiffness is generally smaller than the dynamic measurements due to several factors, including: strain amplitude, dispersion, saturation, anisotropy and relevant rock volume. As pointed out by Fjær, Stroisz and Holt (2013), careful design of experiments may eliminate all of the factors except the strain amplitude effect. As observed for

several rock types, the difference between static and dynamic mechanical compliance increases linearly with stress amplitude during triaxial unloading. This allows for simple linear extrapolation of the measured compliance to zero stress (the point where unloading started), where the extrapolated value corresponds to zero strain amplitude. Any remaining difference between the zero-strain static compliance and the dynamic compliance is believed to reflect dispersion between the frequencies corresponding to the strain rates of a static and a dynamic measurements:

$$\langle \dot{\varepsilon} \rangle = \frac{1}{T} \int_0^T |\dot{\varepsilon}| dt = 4 f \varepsilon_0, \tag{22}$$

here f is the frequency, ε_0 is the strain amplitude associated with an elastic wave, and $T = 1/f$.

The result of applying this method is shown in Figure 3 (e). The compliance, $d\varepsilon_{ax}/d\sigma_{ax}$, is plotted as a function of unloading stress, $\Delta\sigma_{ax}$, and extrapolated towards zero stress leading to the zero-strain limit of Young's modulus $E_{zero\text{-}strain} = [d\varepsilon_{ax}/d\sigma_{ax}(\Delta\sigma_{ax} = 0)]^{-1} = 6.9$ GPa. This zero-strain extrapolated Young's modulus agrees well with the dynamic Young's modulus measured at 1 Hz. Since the strain rate used during triaxial unloading phase of our experiment ($\sim 4 \cdot 10^{-7} s^{-1}$) roughly corresponds to that of a 1 Hz elastic wave in our test ($\sim 2,0 \cdot 10^{-6} s^{-1}$), this result suggests that indeed the difference between static and dynamic Young's modulus at a given frequency originates from both strain effect and dispersion effects (Holt et al. 2015). It also confirms that in some cases dynamic stiffness can be obtained from quasi-static measurements.

The vertical Poisson's ratio (ν_{VH}) shown in Figure 3 (b) does not exhibit large stress sensitivity during CMS loading. For seismic frequencies, it changes by around 0.01 under CMS loading. At ultrasonic frequencies, ν_{VH} of Pierre shale exhibits even smaller stress sensitivity. Measured values are slightly lower than for seismic frequencies and stable at both stress states. Usually, an increase in Poisson's ratio from seismic to ultrasonic frequencies is observed (e.g. Hofmann 2006; Pimenta et al. 2015). It should be noted however, that the values of Thomsen parameters used for anisotropic corrections were obtained during tests performed at different stresses, which may introduce error (see discussion section).

Figure 3 (c,d) shows data obtained during second CMS loading (indicated with numbers 3 and 4 in Figure 2i). The values of Young's modulus at seismic and ultrasonic frequencies are systematically higher than during the first CMS cycle (see Table 1) which is expected to be seen due to the sample over-consolidation. Note that during second CMS loading cycle, at both seismic and ultrasonic frequencies, increase of the vertical Young's modulus is similar to the case of first loading cycle. This indicates that the measured stress sensitivity of Pierre shale (in absolute values) during CMS loading is not affected by material consolidation. Changes in vertical Poisson's ratio are also similar to the one obtained during the first loading cycle (see Table 1). After first CMS unloading the acquired values did not show any considerable change. Slightly smaller increase of Poisson's ratio was observed after the second CMS loading, however, differences are within the experimental errors.

3.2. Wave velocities

Vertical P- and S-wave velocities obtained during both loading cycles are shown in Figure 4 and summarized in Table 1. Ultrasonic velocities were measured directly while seismic velocities were calculated from the measured Young's moduli and Poisson's ratios, assuming stress independent Thomsen parameters ($\varepsilon \approx 0.01, \gamma \approx 0.03, \delta \approx 0.04$; White et al. 1983).

[Figure 4 about here]

Measurements performed at the reference stress exhibit around 22% dispersion in vertical P-wave velocity. First CMS loading shows that the P-wave stress sensitivity is different at low and high frequency regimes. While a large increase of V_{PV} was observed at seismic frequencies, ultrasonic measurements revealed only a small velocity increase upon loading (see Table 1). We define a stress-sensitivity factor and strain-sensitivity factor by:

$$S_{PV} = \frac{\Delta V_{PV}}{V_{PV}\Delta\sigma_z}, \tag{23}$$

$$R_{PV} = \frac{\Delta V_{PV}}{V_{PV}\Delta\varepsilon_z}, \tag{24}$$

with ε_z being the axial strain and σ_z being the axial stress. Both stress-sensitivity and strain-sensitivity factors are about 5 times higher at seismic frequencies compared to ultrasonic frequencies. The S-wave velocity exhibits smaller stress-sensitivity than a P-wave. At the reference stress, vertical S-wave velocities exhibit around 15% dispersion. Again CMS loading caused different increase of S-wave velocities at seismic and ultrasonic frequencies. As a consequence, dispersion decreased slightly. Different stress sensitivity of P- and S-waves results in a distinct V_P/V_S evolution at various frequencies (see Fig. 4e). In the seismic regime, the V_P/V_S changes are about 5-6 times larger than at ultrasonic frequencies (see Fig. 4f). Note that unloading in the first CMS cycle reduces the V_P/V_S ratio almost to its original values despite rather large irreversible changes in V_P and V_S. At seismic frequencies, the CMS unloading to the reference stress, induces a reduction of V_{PV} and V_{SV}. The measured velocities are however higher than those measured at the reference stress before the first CMS cycle. At ultrasonic frequencies we also observe a small increase in absolute values of P- and S-wave velocities after CMS unloading, but the effect is about 4-5 times smaller than for seismic frequencies (see Table 1). During the second CMS cycle, S-wave velocities show a stress-sensitivity comparable to the one measured during the first loading cycle, for both seismic and ultrasonic frequencies. As a consequence dispersion does not change significantly. Also, P-wave velocity measurements roughly reproduce values obtained after the first CMS loading. During the second CMS loading, we again observe rather large stress sensitivity at seismic frequencies and a much smaller sensitivity at ultrasonic frequencies, leading to reduced dispersion. The average velocity change with stress (S_{PV}) during second loading decreased with respect to those of the first loading cycle for both frequency ranges. The strain-sensitivity factors, on the other hand, slightly increased when compared with the previous loading. Finally the V_P/V_S changes during second loading cycle are comparable with the one obtained during initial loading and their absolute values are reproduced with an accuracy of ±0.05.

[Table 1 about here]

4   Discussion

4.1. Effect of frequency dependent stress sensitivity

Presented experimental studies aim to demonstrate how the stress changes caused by an injection into a reservoir influence the mechanical properties of overburden shales for monitoring purposes. It has been observed that velocities and stiffnesses of shales exhibit significant seismic dispersion, and available rock physics models are not always capable of capturing the observed phenomena (Müller, Gurevich and Lebedev 2010). Therefore, the applicability of ultrasonic laboratory tests to seismic field measurements is questionable. For a better understanding of dispersion effects, we have performed experiments at seismic and ultrasonic frequencies. The obtained results indicate that also stress sensitivity of velocities in clay rich materials strongly depend on frequency. In situations where pore-pressure changes in a reservoir influence a thick zone above the reservoir, the effect of dispersive stress-sensitivity on the interpretation of 4D seismic data would be significant. Numerical simulations (Kenter et al. 2004) indicate that in case of a 100 m thick reservoir the influence of a pore-pressure change may affect a zone up to 1000 m above the injection site. In such case, based on measurements performed during first CMS loading, the modelled change in P-wave two-way travel time would differ by a factor of 5 depending on whether stress-sensitivities obtained from seismic or ultrasonic measurements are taken into account. Data acquired during the second CMS cycle exhibits smaller difference between seismic and ultrasonic stress-sensitivities; however, the changes in travel time would still differ by a factor of~ 4.

4.2. Representativeness of laboratory tests for in-situ studies

Presented experiment were conducted on Pierre shale core plugs drilled from outcrop material. Even though Pierre shale is considered as an analogue for overburden rocks, such materials are obviously not fully representative for in-situ situations. Coring the samples and associated stress release could influence their mechanical properties (Holt, Brignoli and Kenter 2000) and make measured responses to differ from in-situ behaviour. Also, in contrast to the present experiments, in

a real case, there is usually a stiffness contrast between reservoir and overburden, which results in overburden stress paths that differ from a CMS loading. It is known that velocities are not only stress dependent but also stress-path dependent. We have recently showed (Holt et al. 2016) that velocities in shales near in-situ stresses are characterized by monotonous (linear) dependence on stress path. In a real field case, inhomogeneities in rocks elastic properties, rock plasticity, and the real geometry of reservoir and overburden formations should be taken into account, and the appropriate stress path should be determined by numerical modelling.

Finally, Thomsen's parameters used to convert between velocities and rock engineering parameters, were not measured directly during our experiments; which obviously introduces an additional error. To this end, it should be noted that: (i) properties of Pierre shale I including Thomsen's parameters differ depending on the shale origin (e.g. Schultz et al. 1980); (ii) Thomsen's parameters are dispersive and may be affected, among others, by stress applied to the sample, loading path, saturation and stress history. Ultrasonic Thomsen's parameters used in this paper were obtained with core plugs drilled from the same batch of material as used in the present work (Holt et al. 2015). However, measurements performed by Holt et al. (2015) were conducted at slightly higher stresses (25 MPa confining pressure, 30 MPa axial stress, and about 12 MPa pore pressure) than those used in our experiments, which could lead to a change of the Thomsen's parameters value. Thomsen's parameters at seismic frequencies were taken from Pierre shale field measurements performed by White et al. (1983) at 950 ft depth. White et al. (1983) do not comment on saturation, engineering parameters, in-situ stresses, or density of their shale. However, suggested by White et al. (1983) density of 2.25 g/cm^3 is smaller than the density of Pierre shale used in present study (2.39 g/cm^3). Based on the velocity data published by White et al. (1983), the vertical Poisson's ratio, v_{VH}, of the field shale was 0,397, which is in good agreement with our measurements. Taking into account the large saturation sensitivity of Poisson's ratio in shales (e.g. Szewczyk, Bauer and Holt 2017b, Vales et al. 2004), it is reasonable to assume that the field shale was fully saturated, as the sample used in the present study. The dynamic vertical Young's modulus, E_V, of the Pierre field shale was 5.3 GPa,

about 1.7 GPa smaller than E_V of our sample. Young's modulus in Pierre shale however, strongly increases with increasing stress experienced by the material (e.g. Szewczyk et al. 2017a). Bearing in mind that under normal pressure conditions, effective stress used in our experiment corresponds to a depth of about 1000 m, which is significantly deeper than the shale formation studied by White et al. (1983), the discrepancy between Young's modulus values, can be attributed to the difference in stress. In addition, the fact that Thomsen's parameters obtained by White et al. (1983) correspond to a lower stress could mean that Thomsen's parameters are slightly different in the present case. Qualitatively, the dependence of Thomsen's parameters on stress and stress path can be deduced from Szewczyk et al. (2017 a, b) and Holt et al. (2016). The sensitivity of conversion between seismic and ultrasonic parameters measured in this work to Thomsen's parameters ε, γ and δ is illustrated in Figure 5.

[Figure 5 about here]

Figure 5 shows, that the conversion from ultrasonically measured vertical velocities to rock engineering parameters, is more sensitive to Thomsen's parameters than conversion from low frequency laboratory measurements of E and ν to velocities. The converted data are particularly sensitive to ε and δ. In the vicinity of the values used in this work, while converting from velocities to engineering parameters, 0.02 variation in ε value causes around 5% difference in the vertical Young's modulus, E_V, and about 4% difference in the vertical Poisson's ratio, ν_{VH}. Similar variation of the δ parameter creates around 6% difference in E_V, and about 2% difference in ν_{VH}. The influence of the variations of the γ parameter are below 1% for both Young's modulus and Poisson's ratio. While converting from rock engineering parameters to velocities, the effects of similar variation of Thomsen's parameters are on average 2-3 times smaller.

4.3. Possible leakage from reservoir

Pierre shale used in our experiment was tested in fully brine saturated conditions. In the field case, there could be some gas partially saturating the caprock (e.g. due to a leakage from the

reservoir). In case of CO_2 storage, leakage from the storage site is a concern, and suitable and reliable monitoring methods are required. Here we present possible effects of CO_2 leakage on 4D seismic attributes.

Common way used in geophysics for identifying effects of fluid substitution in conventional reservoirs involves use of the Gassmann model (Gassmann 1951). Many of the assumptions underlying the Gassmann model are violated in shales during any field or laboratory investigations. Real shales are heterogeneous, composed of several minerals and the pore connectivity is rather poor. Increased volume of the shale pore fluid at seismic frequencies causes strong softening of the frame and changes the shear moduli (Szewczyk et al. 2017b). Water near the clay surfaces influence the rock physical properties (Holt and Kolstø 2017). Moreover, due to observed dispersion (Figures 3 and 4), the shale is often unrelaxed or only partially relaxed even at seismic frequencies. Nevertheless, as shown elsewhere (Szewczyk et al. 2017b), the anisotropic Gassmann model may still be applicable for seismic velocities in shales if modifications accounting for the rock-fluid interaction effects, such as adsorption effects leading to frame weakening (e.g. Spencer 1981; Murphy et al. 1984; Moerig et al. 1996) and capillary-pressure effects, are introduced into the model. The equations of modified anisotropic Gassmann model accounting for the adsorption driven frame weakening are:

$$C_{IJ}^{eff} = (1 - aS_w)C_{IJ}^{fr} + \frac{\alpha}{D^*}b_I b_J, \tag{25}$$

$$b_I = \beta_I - \frac{(1 - aS_w)(C_{1I}^{fr} + C_{2I}^{fr} + C_{3I}^{fr})}{3K_s}, \tag{26}$$

$$\beta_1 = \beta_2 = \beta_3 = 1, \tag{27}$$

$$\beta_4 = \beta_5 = \beta_6 = 0, \tag{28}$$

$$\frac{1}{\alpha} = \varphi\left(\frac{1}{K_f} - \frac{1}{K_s}\right), \tag{29}$$

$$D^* = 1 + \frac{\alpha}{3K_s}(b_1 + b_2 + b_3), \tag{30}$$

where the index fr denotes the properties of frame, K_f and K_s stands for the bulk modulus of pore fluid and solid phase, respectively, φ indicates the porosity, C_{ij} represent the independent elements of stiffness tensor, S_w is the wetting phase saturation, and a is fitting parameter accounting for the fluid phase driven frame weakening through adsorption effects. The capillary pressure effects at microscopic scale on the other hand, may be accounted for by calculating the effective fluid modulus through Brie's mixing law (e.g. Santos et al. 1990; Papageorgiou et al. 2016). The Brie's empirical equation (Brie et al. 1995) follows:

$$K_{f,Brie} = \left(K_{f,liquid} - K_{f,gas}\right)\left(1 - S_{gas}\right)^e + K_{f,gas} \tag{31}$$

where S_{gas} stands for non-wetting phase saturation, $K_{f,liquid}$ and $K_{f,gas}$ are bulk moduli of wetting and non-wetting phases, respectively, while e is an adjustable parameter which in case of high values would move the effective fluid modulus towards Reuss average and in case of low values towards Voigt average. The use of Gassmann model requires anisotropic frame properties. In the present work, the frame properties were estimated in such a way that the modified Gassmann model reproduces values measured for full brine saturation. The effective bulk modulus of solid phase ($K_s = 24\ GPa$), Brie's adjustable parameter (e=2,4), and parameter a accounting frame weakening (a=0,36) of Pierre shale were taken from Szewczyk et al. (2017b). We have considered a two-phase fluid system filling up the pore space (brine and CO_2). The bulk modulus and density of brine were $K_{f,brine} = 2.6\ GPa$ and $\rho_{brine} = 1.035\ g/cm^3$, respectively, (e.g. Batzle and Wang 1992) while bulk modulus and density of CO_2 were $K_{f,CO_2} = 0.004\ GPa$ and $\rho_{CO_2} = 0.624\ g/cm^3$ (e.g. Burke 2011). Being aware that CO_2 properties are affected by pressure and temperature we decided to keep them constant, since bulk modulus and density of CO_2 are low compared to those of brine; thus accounting for pressure and temperature dependence would have only a small impact on the final results.

Figure 6 (a) shows vertical P-wave velocities as a function of CO_2 saturation calculated based on seismic (1 Hz) measurements performed at all examined stress states.

[Figure 6 about here]

The modelled effect of gas saturation (in relative terms) is quite similar during first and second CMS cycles. The modelling of the fluid substitution indicates that the small leakages of the CO_2 into the overburden formation would create noticeable travel time shifts, under the assumption that the overburden formation was initially fully brine saturated. 10% CO_2 saturation in the overburden due to possible leakage could create up to 3% P-wave velocity change. Obviously, possibility of detecting such events during 4D surveys depends on the related changes of the two-way travel times, and thus on the length of CO_2 penetration into the shale formation. Assuming good quality data, current 4D detection limit for changes of the two-way travel time is below 1 ms (e.g. Landrø et al. 2017). Using vertical P wave velocities from our 1Hz data (about 2500 m/s) and assuming 3% velocity change due to the CO_2 leakage, this threshold would be reached after the CO_2 has propagated for about 40 m into the overburden formation, which is quite likely in the case of the overpressured reservoirs (e.g. during CO_2 injection for storage or EOR). The fluid substitution effects are visible up to about 50%-60% gas saturation. Afterwards, the changes of the velocities are mainly controlled by the adsorption effects present in shales and leading to the weakening of anisotropic frame moduli (those effects may have magnitude comparable with the fluid substitution effects). This can be seen by the drop of seismic velocities while going from fully gas saturated shale up to about 30-40% fluid saturation and increase of the velocities afterwards (similar behaviour was observed experimentally in Szewczyk et al. 2017b). Another interesting observation is that the CMS loading seems to decrease the range in which fluid substitution effects are dominant (compare black and grey curves in Figure 6a). Note also, that the P-wave velocity changes associated with fluid substitution may be of comparable magnitude as one associated with a stress change: based on seismic data obtained at reference stress 10% CO_2 saturation would lead to a velocity change comparable to that obtained by about 1,9 MPa shear stress change during CMS loading.

Velocity changes associated with fluid substitution are clearly stress dependent (additional load decreases fluid phase sensitivity). Moreover, fluid substitution effects depends on the material hysteresis. This is further shown in Figure 6b where the shear stress sensitivity of vertical P-wave

velocities ($\frac{\Delta V_P}{\sigma_z - \sigma_R}$) is plotted as a function of CO_2 saturation. In absolute values, during initial CMS

loading the seismic stress sensitivity reduces from 115 m/s MPa^{-1} to 38 m/s MPa^{-1} when going from

full CO_2 saturation to full brine saturation. For the second CMS cycle, the seismic stress sensitivity of

the P-wave velocity decreases from 95 m/s MPa^{-1} to 28 m/s MPa^{-1}. Note however, that in the relative

values the stress sensitivity at seismic frequencies is about 3 times higher in case of full CO_2

saturation than in case of full brine saturation regardless loading cycle (during first CMS loading

stress sensitivity reduces by ~ 67%, while during second CMS loading by ~ 70%).

5   Conclusions

Pierre shale I (mimicking caprock) was subjected to laboratory tests evaluating expected

mechanical and acoustic responses of the overburden formation to fluid injection into reservoir

beneath it (e.g. for CO_2 storage or enhanced recovery). Outcrop core plugs were tested in drained

condition, with 3.5% NaCl brine as a pore fluid, and under constant pore pressure. The experiments

were carried out in set-up allowing for quasi-static rock deformation measurements, ultrasonic

velocity determination and quantification of the sample responses at seismic frequencies. In addition

possible fluid substitution effects were simulated with the use of modified anisotropic Gassmann

model.

Our experiments at seismic and ultrasonic ranges reveal big frequency dependence of elastic

moduli and wave velocities, thus demonstrating significance of low-frequency laboratory studies. The

observed stress sensitivity of the shale was higher at seismic frequencies, indicating importance of

accounting for the dispersion effects during seismic data interpretation based on ultrasonic

laboratory measurements. Injection into reservoir increases overburden Young's modulus and

acoustic P- and S-wave velocities, and would create significant travel time reduction. Repeated CMS

loading reveals that elimination of the non-elastic effects decrease the stress sensitivity, increase the

acoustic velocities, and stiffer the sample. The observed phenomena are in qualitative agreement

with field observations however, care needs to be taken while generalizing those results due to

limitations of applied procedures and possible differences in material properties. Nevertheless, the experiments point out possible mechanisms that should be accounted for during geomechanical or 4D seismic modelling of injection scenarios. Simple poroelastic modelling of the fluid substitution (based on the modified Gassmann model) demonstrate that relatively small leakages of the CO_2 into the overburden rock may lead to velocity changes which are comparable with those induced by stress modifications. Both the geomechanical and the fluid substitution effects would create significant time shifts which could be detected with 4D seismic. Presented quasi-static measurements indicates, as claimed by others, that the differences between static and dynamic moduli are due to both strain-amplitude and dispersion effects, and that correct experimental procedure allow in some cases to obtain dynamic stiffness from quasi-static measurements.

6 Acknowledgments

References

Barkved O.I. and Kristiansen T. 2005. Seismic time-lapse effects and stress changes: Examples from a compacting reservoir. The Leading Edge 24, 1244–1249.

Batzle M. and Wang. Z. 1992. Seismic properties of pore fluids. Geophysics 57, 1396-1408.

Batzle M., Hofmann R., Prasad M., Kumar G., Duranti L. and Han D. 2005. Seismic Attenuation: Observations and Mechanisms. 2005 SEG Annual Meeting, Houston, USA, SEG-2005-1565.

Batzle M., Han D. and Hofmann R. 2006. Fluid mobility and frequency-dependent seismic velocity — Direct measurements. Geophysics 71, (1), N1-N9.

Brie A., Pampuri F., Marsala A.F. and Meazza O. 1995. Shear Sonic Interpretation in Gas-Bearing Sands. 1995 SPE Annual Technical Conference and Exhibition, Dallas, USA.

Burke L. 2011. Carbon dioxide fluid-flow modeling and injectivity calculations.Scientific Investigation Report 20115083 U.S. Department of the Interior.

Cole K. S. and Cole R. H. 1941. Dispersion and Absorption in Dielectrics - I Alternating Current Characteristics. The Journal of Chemical Physics 9, 341–352.

Duffaut K. and Landrø M. 2007. Vp/Vs ratio versus differential stress and rock consolidation – A comparison between rock models and time-lapse AVO data. Geophysics 72, (5), C81–C94.

Duranti L., Ewy R. and Hofmann R. 2005. Dispersive And Attenuative Nature of Shales: Multiscale And Multifrequency Observations. 2005 SEG Annual Meeting, Houston, USA, SEG-2005-1577.

Fjær E., Stroisz A., and Holt R. M. 2013, Elastic dispersion derived from a combination of static and dynamic measurements. Rock Mechanics and Rock Engineering 46, 611-618.

Gassmann F. 1951. Elasticity of porous media. Vierteljahrschrift der Naturforschenden Gesellschaft in Zürich, 96, 1 – 23 (in German).

Geertsma J. 1973. A basic theory of subsidence due to reservoir compaction: The homogeneous case. Verhandelingen Koninklijk Nederlands Geologisch Mijnbouwkundig Genootschap 28, 43–62.

Gordon R.B. and Davis L. A. 1968. Velocity and attenuation of seismic waves in imperfectly elastic rock. Journal of Geophysical Research 73, (12), 3917-3935.

Hatchell P. and Bourne S. 2005. Rocks under strain: Strain-induced time lapse shifts are observed for depleting reservoirs. The Leading Edge 24, 1222–1225.

Helbig, K. 1994. Foundations of Anisotropy for Exploration Seismics, 1st Edition, Elsevier.

Hofmann R. 2006. Frequency dependent elastic and anelastic properties of clastic rock. PhD thesis at Colorado School on Mines, Golden, USA.

Holt R.M., Brignoli M. and Kenter C.J. 2000. Core quality: Quantification of coring-induced rock alteration. International Journal of Rock Mechanics 37, 889–907.

Holt R. M. and Stenebråten J. F. (2013), Controlled laboratory experiments to assess the geomechanical influence of subsurface injection and depletion processes on 4D seismic responses. Geophysical Prospecting 61, 476–488.

Holt R.M., Bauer A., Fjaer E., Stenebråten J.F., Szewczyk D. and Horsrud P. 2015. Relating Static and Dynamic Mechanical Anisotropies of Shale. 49th U.S. Rock Mechanics/Geomechanics Symposium, San Francisco, USA, ARMA-2015-484.

Holt R.M., Bauer A., Bakk A. and Szewczyk D. 2016. Stress-path dependence of ultrasonic and seismic velocities in shale. SEG Technical Program Expanded Abstracts 2016, 3159-3163.

Holt R.M. and Kolstø M.I. 2017. How does water near clay mineral surfaces influence the rock physics of shales? Geophysical prospecting (in press).

Islam M. A. and Skalle P. 2013. An experimental investigation of shale mechanical properties through drained and undrained test mechanisms. Rock Mechanics and Rock Engineering 46, 1391-1413.

Iwasaki T., Tatsuoka F. and Takagi Y. 1978. Shear moduli of sand under cyclic torsional shear loading. Soils and Foundation 18, (1), 39-56.

Johnston J. E. and Christensen N. I. 1995. Seismic anisotropy of shales. Journal of Geophysical Research: Solid Earth 100(B4): 5991-6003.

Kenter C.J., Van den Beukel A.C., Hatchell P.J., Maron K.P., Molenaar M.M. and Stammeijer J.G.F. 2004. Geomechanics and 4D: Evaluation of reservoir characteristics from time shifts in the overburden. ARMA/NARMS 04-627. Proceedings of Gulf Rocks 2004, Houston, USA, 8 pp.

Landrø M., Veire H. H., Duffaut K. and Najjar, N. 2003. Discrimination between pressure and fluid saturation changes from marine multicomponent time-lapse seismic data. Geophysics 68, (5), 1592-1599.

Landrø M. and Amundsen L. 2017. Time-Lapse Seismic and Geomechanics - Part I. GeoExPro 14 (2), 46-49.

Lumley D. 2010. 4D seismic monitoring of CO 2 sequestration. The Leading Edge 29, (2), 150-155.

Mavko G., Mukerji T. and Dvorkin J. 2009. The Rock Physics Handbook. 2nd ed. Cambridge: Cambridge University Press.

Mavko G. and Vanorio. T. 2010. The influence of pore fluids and frequency on apparent effective stress behavior of seismic velocities. Geophysics 75, (1), N1-N7.

Meadows M. 2008. Time-lapse seismic modeling and inversion of CO_2 saturation for storage and enhanced oil recovery. The Leading Edge 27, (4), 506-516.

Mikhaltsevitch V., Lebedev M. and Gurevich B. 2014. A laboratory study of low-frequency wave dispersion and attenuation in water-saturated sandstones. The Leading Edge 33, 616-622.

Moerig R., Waite W. F., Boyd O. S., Getting I. C. and Spetzler H. A. 1996. Seismic attenuation in artificial glass cracks: Physical and physicochemical effects of fluids. Geophysical Research Letters 23, 2053-2056.

Müller T.M., Gurevich B. and Lebedev M. 2010. Seismic wave attenuation and dispersion resulting from wave-induced flow in porous rocks - A review. Geophysics 75, (5), 75A147-75A164.

Murphy W.F., Winkler K.W. and Kleinberg R.L. 1984. Frame modulus reduction in sedimentary rocks: the effect of adsorption on grain contacts. Geophysical Research Letters 11, 805-808.

Nye J. F. 1985. Physical properties of crystals: their representation by tensors and matrices. Oxford: Clarendon.

Olgaard D.L., Nuesch R. and Urai J. 1995. Consolidation of water saturated shales at great depth under drained conditions. Proc. 8th International Congress on Rock Mechanics, Tokyo, Japan, 25-29.

Papageorgiou G., Amalokwu K. and Chapman M. 2016. Theoretical derivation of a Brie-like fluid mixing law. Geophysical Prospecting 64, 1048-1053.

Pimienta L., Fortin J. and Gueguen Y. 2015. Experimental study of Young's modulus dispersion and attenuation in fully saturated sandstones. Geophysics 80, (5), L57-L72.

Santos J.E., Corberó J.M. and Douglas J. 1990. Static and dynamic behavior of a porous solid saturated by a two-phase fluid. The Journal of the Acoustical Society of America 87, 1428-1438.

Schultz L. G, Tourtelot H.A., Gill J.R. and Boerngen J.G. 1980. Composition and properties of the Pierre Shale and equivalent rocks, northern Great Plains region. U.S. Geological Survey professional paper, 1064-B.

Skempton A. W. 1954. The Pore-Pressure Coefficients A and B. Géotechnique 4, 143-147.Spencer J. W. 1981. Stress relaxations at low frequencies in fluid-saturated rocks: Attenuation and modulus dispersion. Journal of Geophysical Research: Solid Earth 86, (B3), 1803-1812.

Suarez-Rivera R., Willson S., Nakagawa S., Nes O. M. and Liu Z. 2001. Frequency scaling for evaluation of shale and mudstone properties from acoustic velocities. AGU 2001 Fall Meeting, San Francisco, USA, T32E-0924.

Szewczyk D., Bauer A. and Holt R. M. (2016), A new laboratory apparatus for the measurement of seismic dispersion under deviatoric stress conditions. Geophysical Prospecting 64, 789–798.

Szewczyk D., Bauer A. and Holt R. M. 2017a. Stress dependent properties of shales – Laboratory experiments at seismic and ultrasonic frequencies. Geophysical Journal International (in press).

Szewczyk D., Bauer A. and Holt R. M. 2017b. The impact of saturation on seismic dispersion in shales - Laboratory measurements at seismic and ultrasonic frequencies. Geophysics (in press).

Thomsen L. 1986. Weak elastic anisotropy. Geophysics 51, (10), 1954-1966.

Vales F., Nguyen Minh D., Gharbi H. and Rejeb A. 2004. Experimental study of the influence of the degree of saturation on physical and mechanical properties in Tournemire shale (France). Applied Clay Science, Volume 26, Issues 1–4, Pages 197-207.

Voigt W. 1928. Lehrbuch der kristallphysik (mit ausschluss der kristalloptik). B.G. Teubner.

Walsh J.B. 1965. The Effect of Cracks on the Uniaxial Elastic Compression of Rocks. J. Geophys. Res. 70, (2), 399–411.

Wang Z. 2002. Seismic anisotropy in sedimentary rocks, part 2: Laboratory data. Geophysics 67, (5), 1423-1440.

White J. E., Martineau-Nicoletis L. and Monash C. 1983. Measured anisotropy in Pierre shale. Geophysical Prospecting 31, 709–725.

Winkler K. and Nur A. 1979. Pore fluids and seismic attenuation in rocks. Geophysical Research Letters 6, (1): 1-4.

List of figures

1.   Figure 1 - Schematic drawings of the experimental setup (a), the sample with attached foil strain gages measuring strains in axial and radial directions (b), and the orientation (relative to the bedding planes, indicated by dashed lines) of tested sample together with the P- and S-waves propagation and particle motion directions (c). Indicated on the drawings are: piston (A), pressure vessel (B), linear variable displacement transducers (LVDT's) measuring axial quasi-static deformations (C), adapter plates holding the LVDTs (D), aluminum standard with attached strain gages for phase shift measurements at seismic frequencies (E), piezoelectric force sensor measuring force modulations at seismic frequencies (F), piezoelectric actuator generating displacement modulations at seismic frequencies (G), internal load cell measuring deviatoric stress (H), top and bottom endcaps with embedded compressional and shear wave transducers, and a pore-fluid lines (I), sample (J), strain gages attached to sample for a measurements of quasi-static and dynamic strains (K), rubber sleeve sealing the sample from the oil used for applying confining pressure (L), and pore-fluid lines (M).

2.   Figure 2 – (a-h) Pierre shale I ultrasonic waveforms acquired after sample stabilization during two subsequent CMS loading cycles indicated in (i). (i) Stress path applied to sample during the tests. Numbers indicate times of specific measurements: 1-4 dynamic measurements at seismic and ultrasonic frequencies; 5 quasi-static measurements (triaxial unloading).

3.   Figure 3 – Dynamic and quasi-static rock mechanical properties of Pierre shale I obtained during both CMS cycles and during triaxial unloading. Numbers in circles corresponds to the measurements points indicated in Figure 2i. (a) Seismic dispersion of dynamic vertical Young's modulus obtained during initial CMS loading, as well as quasi-static Young's modulus obtained during triaxial unloading and the zero-strain limit of the quasi-static Young's modulus. (b) Dispersion of vertical Poisson's ratio measured during initial CMS loading. (c,d) Analogical set of data obtained during second CMS loading where the effects of non-elastic deformations may be noticed. (e) Axial

compliance of the stress-strain curve measured during triaxial unloading (a linear fit to the data allows for extrapolation to zero stress/strain limit - Fjær et al. 2013). Solid lines in (a,c) show manual Cole-Cole fits to the experimental data (Cole and Cole 1941). Ultrasonic points were calculated from VP and VS measured perpendicular to bedding by assuming Thomsen anisotropy parameters obtained from different experiments performed on core plugs cut from the same batch as tested here (ε=0.13, γ=0.25, δ=0.10).

4.   Figure 4 – Seismic dispersion of vertical P-and S-wave velocities (a-d), V_{PV}/V_{SV} ratio (e), and change of the V_{PV}/V_{SV} ratio (f) obtained during both CMS cycles. Numbers in circles corresponds to the measurements points indicated in Figure 2i. Velocities at seismic frequencies were calculated from measured E_V and ν_{VH} by assuming Thomsen anisotropy parameters obtained from White et al. (1983) field measurements ($\varepsilon\approx$0.01, $\gamma\approx$0.03, $\delta\approx$0.04).

5.   Figure 5 – Sensitivity of conversion between velocities and rock engineering parameters to Thomsen's parameters. Black symbols indicate conversion from ultrasonically measured vertical velocities to Young's modulus and Poisson's ratio, while gray symbols represent conversion from seismic measurements to velocities. While varying individual Thomsen's parameter (value used in manuscript indicated by vertical lines), the remaining two were fixed to the values used in this work i.e. (i) $\varepsilon \approx 0.01$, $\gamma \approx 0.03$, $\delta \approx 0.04$ for seismic frequencies; and (ii) ε=0.13, γ=0.25, δ=0.10 for ultrasonic frequencies.

6.   Figure 6 – (a) Seismic and ultrasonic vertical P-wave velocities as a function of brine $CO2$ saturation calculated with the use of modified anisotropic Gassmann model. Different stress states are indicated with numbers in circles and corresponds to the measurements points indicated in Figure 2i. (b) Shear stress sensitivity of the vertical P-wave velocity ($\Delta V_{PV}/(\sigma_Z-\sigma_R)$) as a function of $CO2$ saturation for seismic frequencies. Calculations were based on modified anisotropic Gassmann model and laboratory measurements.
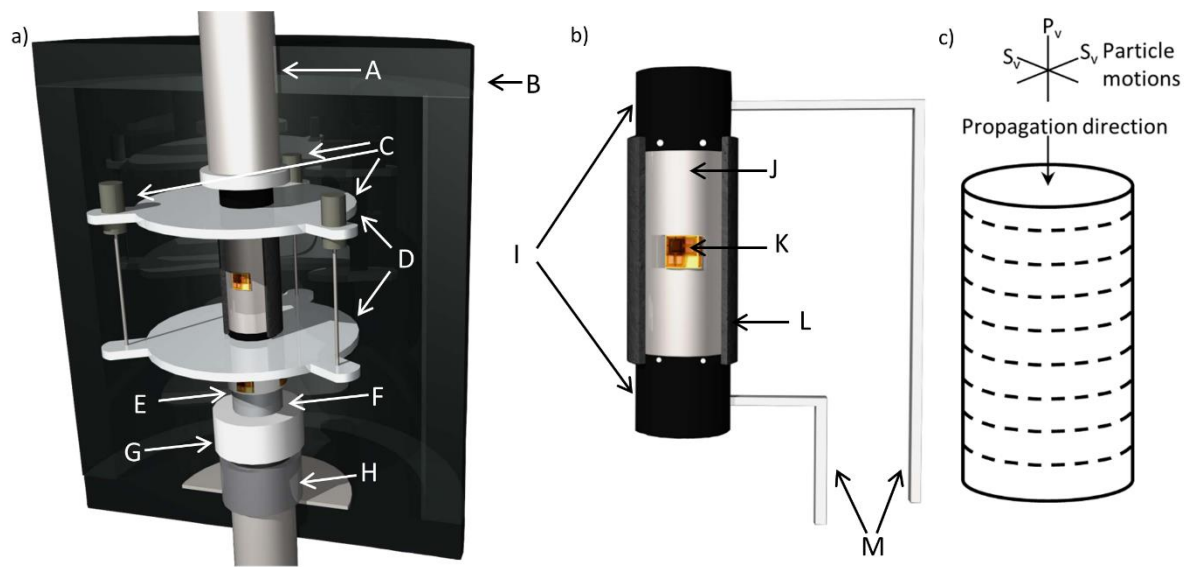
Figure 1 - Schematic drawings of the experimental setup (a), the sample with attached foil strain gages measuring strains in axial and radial directions (b), and the orientation (relative to the bedding planes, indicated by dashed lines) of tested sample together with the P- and S-waves propagation and particle motion directions (c). Indicated on the drawings are: piston (A), pressure vessel (B), linear variable displacement transducers (LVDT's) measuring axial quasi-static deformations (C), adapter plates holding the LVDTs (D), aluminum standard with attached strain gages for phase shift measurements at seismic frequencies (E), piezoelectric force sensor measuring force modulations at seismic frequencies (F), piezoelectric actuator generating displacement modulations at seismic frequencies (G), internal load cell measuring deviatoric stress (H), top and bottom endcaps with embedded compressional and shear wave transducers, and a pore-fluid lines (I), sample (J), strain gages attached to sample for a measurements of quasi-static and dynamic strains (K), rubber sleeve sealing the sample from the oil used for applying confining pressure (L), and pore-fluid lines (M).
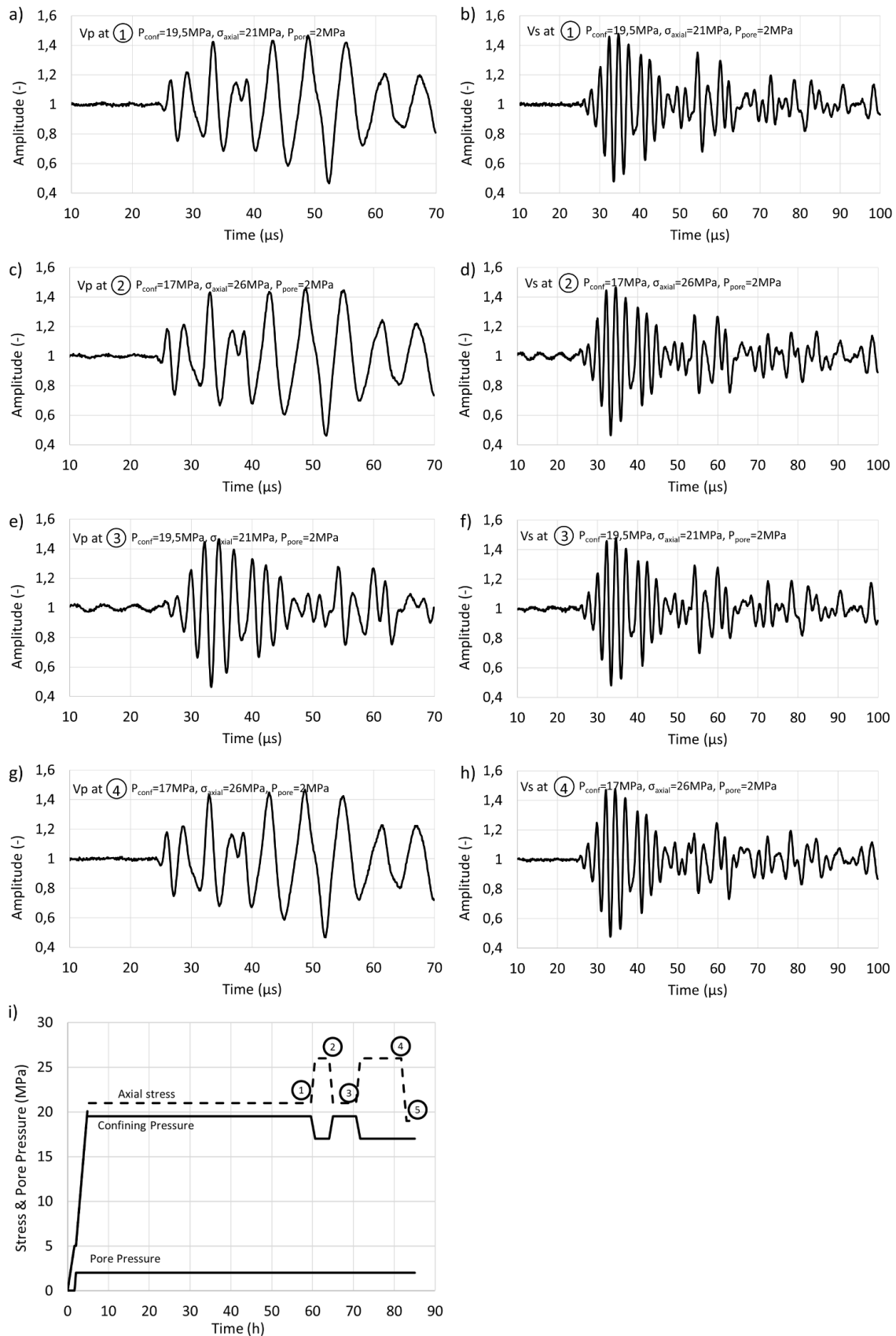
Figure 2 – (a-h) Pierre shale I ultrasonic waveforms acquired after sample stabilization during two subsequent CMS loading cycles indicated in (i). (i) Stress path applied to sample during the tests. Numbers indicate times of specific measurements: 1-4 dynamic measurements at seismic and ultrasonic frequencies; 5 quasi-static measurements (triaxial unloading).
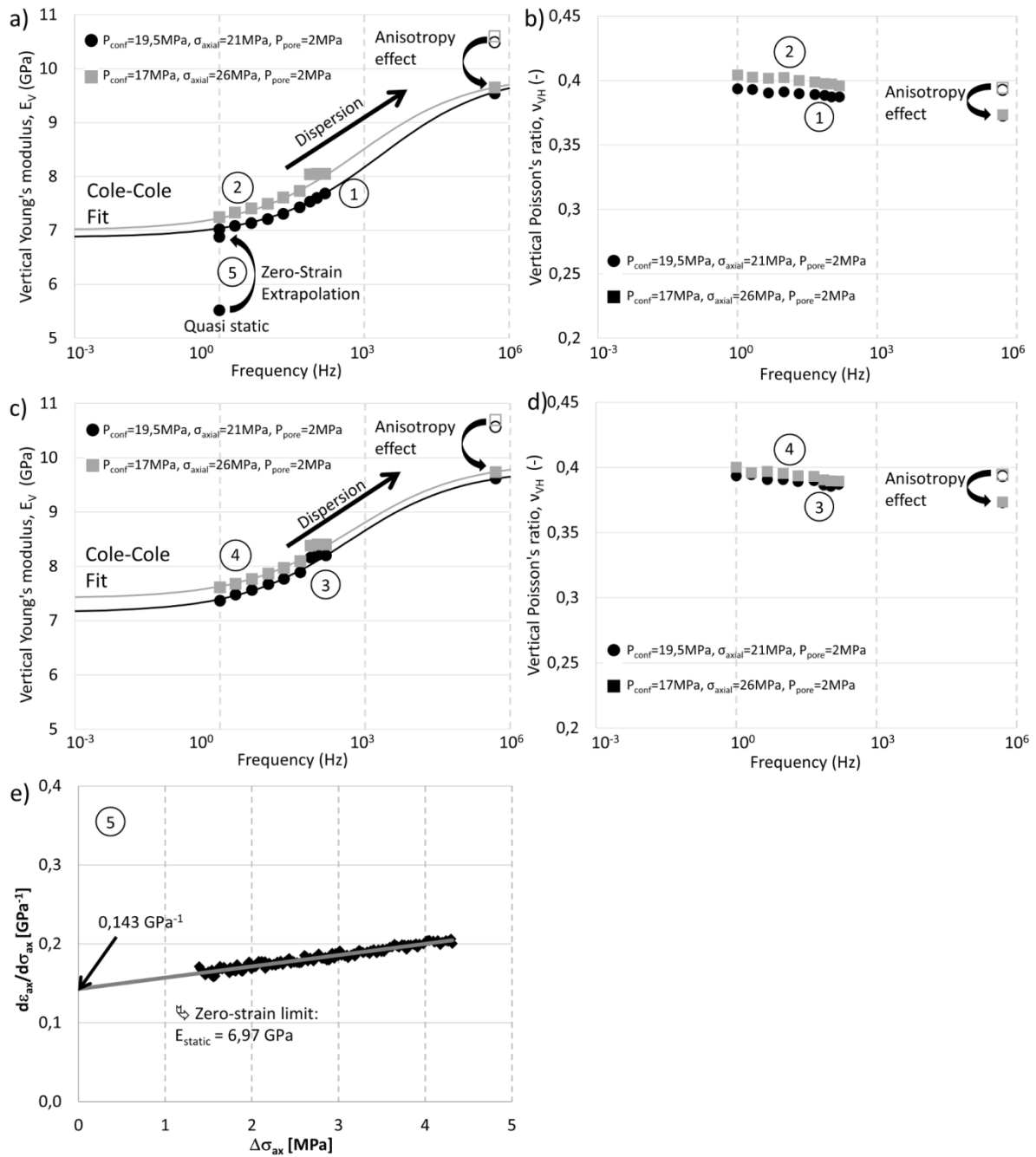
Figure 3 – Dynamic and quasi-static rock mechanical properties of Pierre shale I obtained during both CMS cycles and during triaxial unloading. Numbers in circles corresponds to the measurements points indicated in Figure 2i. (a) Seismic dispersion of dynamic vertical Young's modulus obtained during initial CMS loading, as well as quasi-static Young's modulus obtained during triaxial unloading and the zero-strain limit of the quasi-static Young's modulus. (b) Dispersion of vertical Poisson's ratio measured during initial CMS loading. (c,d) Analogical set of data obtained during second CMS loading where the effects of non-elastic deformations may be noticed. (e) Axial compliance of the stress-strain curve measured during triaxial unloading (a linear fit to the data allows for extrapolation to zero stress/strain limit - Fjær et al. 2013). Solid lines in (a,c) show manual Cole-Cole fits to the experimental data (Cole and Cole 1941). Ultrasonic points were calculated from V_P and V_S measured perpendicular to bedding by assuming Thomsen anisotropy parameters obtained from different experiments performed on core plugs cut from the same batch as tested here ($\varepsilon=0.13$, $\gamma=0.25$, $\delta=0.10$).
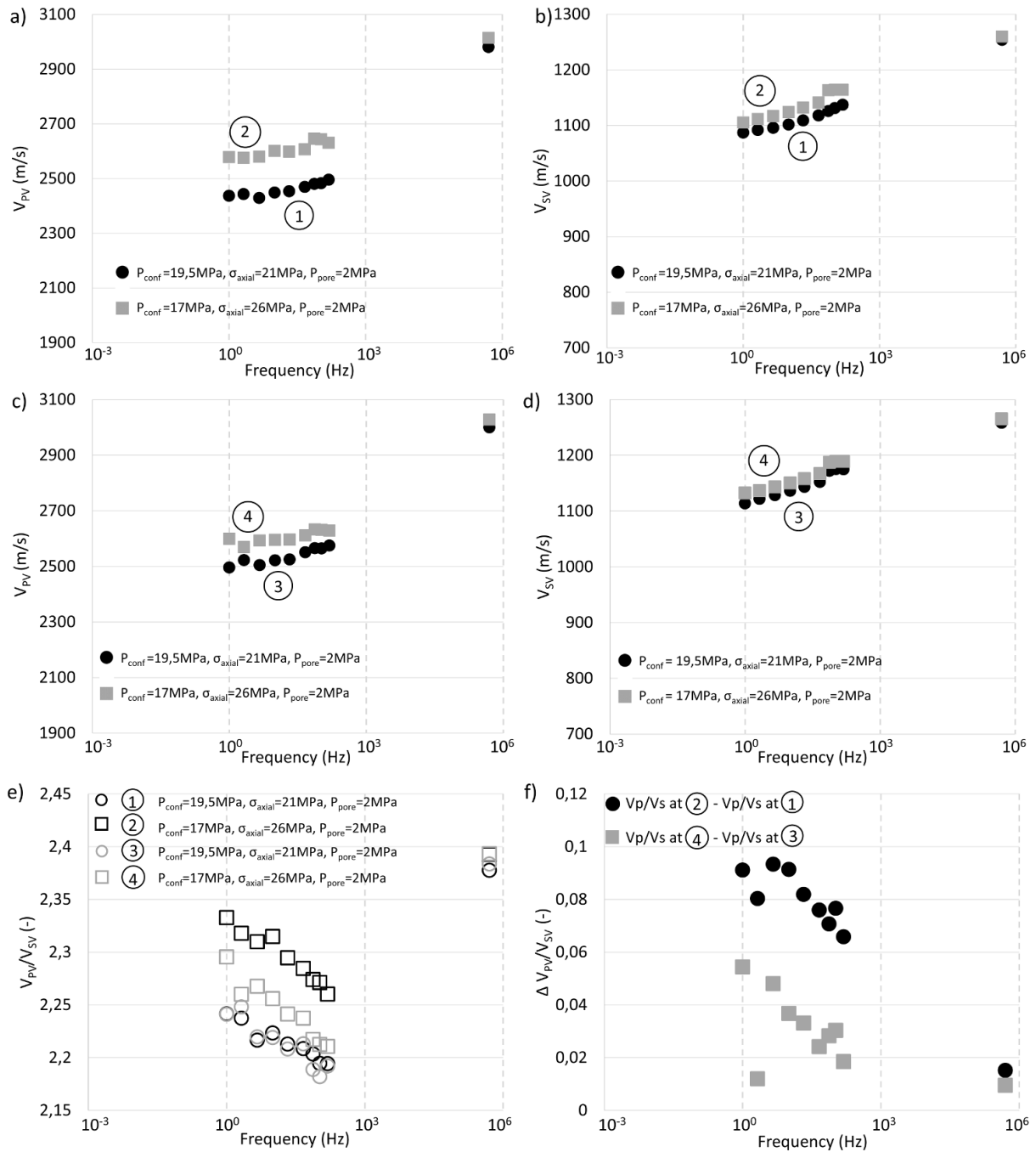
Figure 4 – Seismic dispersion of vertical P-and S-wave velocities (a-d), V_{PV}/V_{SV} ratio (e), and change of the V_{PV}/V_{SV} ratio (f) obtained during both CMS cycles. Numbers in circles corresponds to the measurements points indicated in Figure 2i. Velocities at seismic frequencies were calculated from measured E_V and ν_{VH} by assuming Thomsen anisotropy parameters obtained from White et al. (1983) field measurements ($\varepsilon \approx 0.01$, $\gamma \approx 0.03$, $\delta \approx 0.04$).
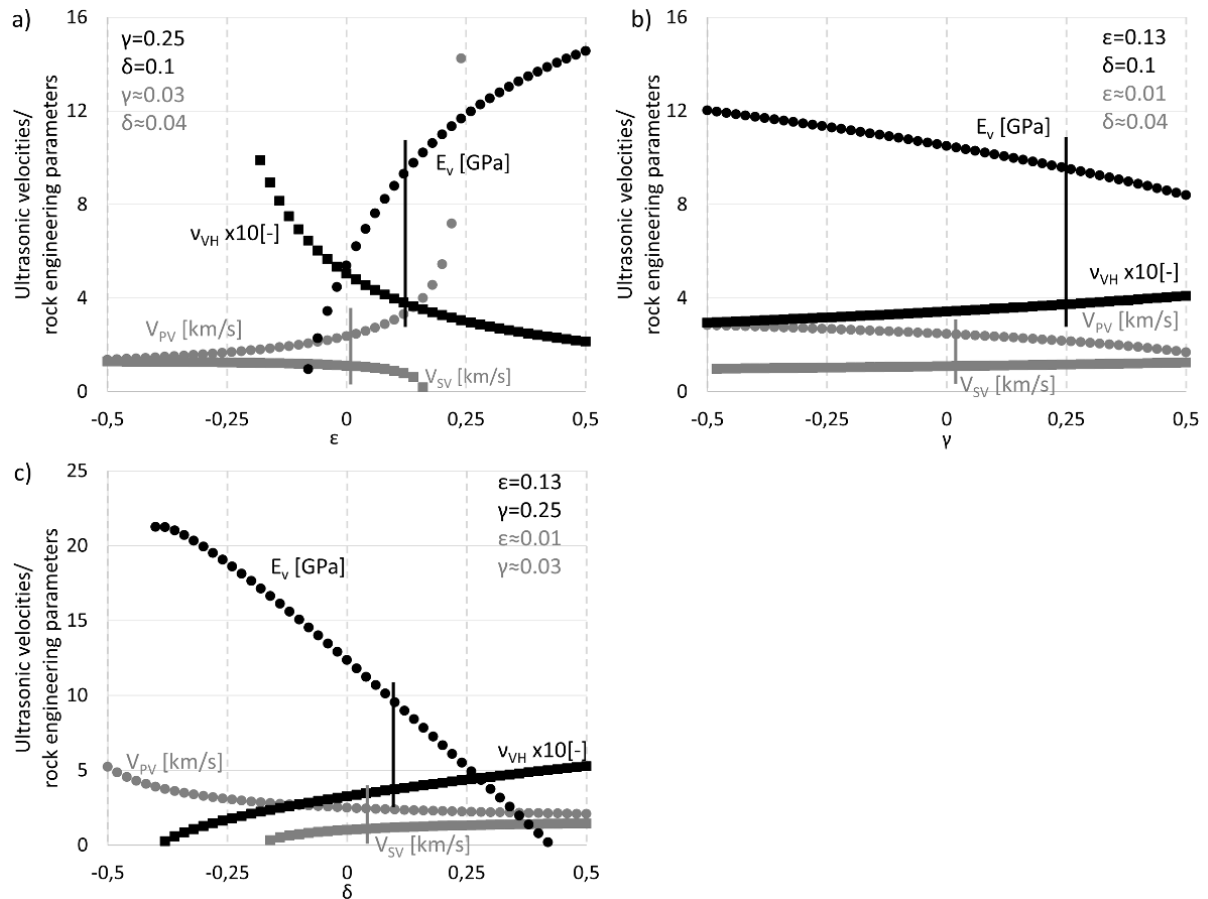
Figure 5 – Sensitivity of conversion between velocities and rock engineering parameters to Thomsen's parameters. Black symbols indicate conversion from ultrasonically measured vertical velocities to Young's modulus and Poisson's ratio, while gray symbols represent conversion from seismic measurements to velocities. While varying individual Thomsen's parameter (value used in manuscript indicated by vertical lines), the remaining two were fixed to the values used in this work i.e. (i) ε ≈ 0.01, γ ≈ 0.03, δ ≈ 0.04 for seismic frequencies; and (ii) ε=0.13, γ=0.25, δ=0.10 for ultrasonic frequencies.
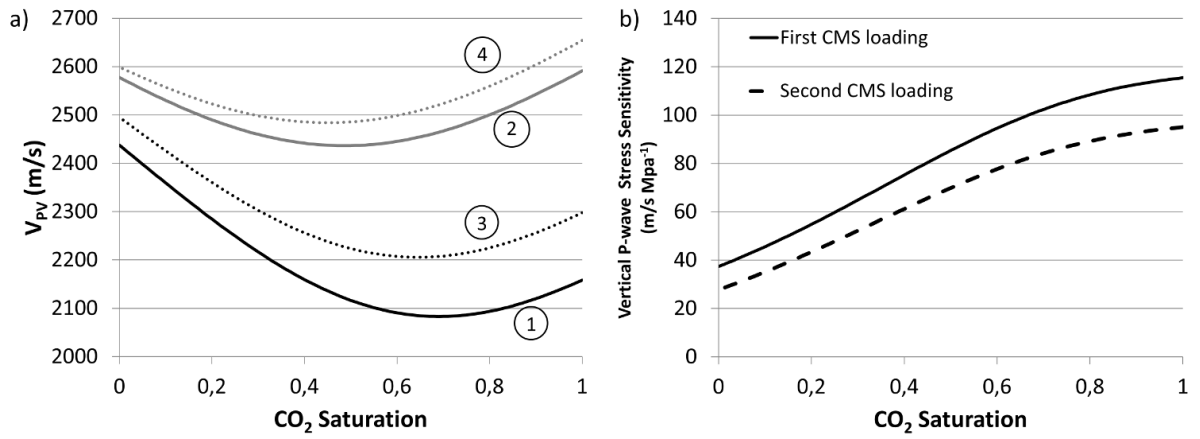
Figure 6 – (a) Seismic vertical P-wave velocities as a function of CO_2 saturation calculated with the use of modified anisotropic Gassmann model. Different stress states are indicated with numbers in circles and corresponds to the measurements points indicated in Figure 2i. (b) Shear stress sensitivity of the vertical P-wave velocity ($\Delta V_P/(\sigma_Z-\sigma_R)$) as a function of CO_2 saturation for seismic frequencies. Calculations were based on modified anisotropic Gassmann model and laboratory measurements.

List of Tables

Table 1 – List of vertical Young's modulus, Poisson's ratio, and vertical P- and S-wave velocities together with their dispersions, V_{PV}/V_{SV} ratio, stress-sensitivity and strain-sensitivity factors obtained during both CMS loading cycles.

	Reference stress		1st CMS loading		Reference stress (repetition)		2nd CMS loading	
	Seismic (1 Hz)	ultrasonic	Seismic (1 Hz)	ultrasonic	Seismic (1 Hz)	ultrasonic	Seismic (1 Hz)	ultrasonic
Vertical Young's modulus, E_V (GPa)	7.03	9.54	7.25	9.65	7.34	9.62	7.62	9.74
E_V dispersion	36%		33%		31%		28%	
Vertical Poisson's ratio, ν_{VH} (-)	0.394	0.373	0.404	0.373	0.394	0.373	0.4	0.373
Vertical P-wave velocity, V_{PV} (m/s)	2443	2981	2578	3014	2496	2999	2599	3028
V_{PV} dispersion	22.0%		16.9%		20.2%		16.5%	
Vertical S-wave velocity, V_{SV} (m/s)	1087	1254	1105	1260	1114	1258	1132	1265
V_{SV} dispersion	15.4%		14.0%		12.9%		11.8%	
V_{PV}/V_{SV} (-)	2.248	2.377	2.333	2.392	2.241	2.384	2.296	2.394
Stress-sensitivity factor, S_{PV} (MPa^{-1})	-	-	$11.5 \cdot 10^{-3}$	$2.4 \cdot 10^{-3}$	-	-	$8.4 \cdot 10^{-3}$	$2 \cdot 10^{-3}$
Strain-sensitivity factor, R_{PV} (-)	-	-	23	4.5	-	-	25	6